Proc. *18th Internat. Conf. on Information Processing in Medical Imaging (IPMI'03)*, Ambleside, UK, 20th - 25th July 2003, In *Lecture Notes in Computer Science*, Springer Verlag Berlin Heidelberg 2003, 76-88, © Springer-Verlag

Localization of Anatomical Point Landmarks in 3D Medical Images by Fitting 3D Parametric Intensity Models

Stefan Wörz, Karl Rohr

School of Information Technology, Computer Vision & Graphics Group
International University in Germany, 76646 Bruchsal
Email: {woerz,rohr}@i-u.de

Abstract. We introduce a new approach for the localization of 3D anatomical point landmarks based on 3D parametric intensity models which are directly fit to the image. We propose an analytic intensity model based on the Gaussian error function in conjunction with 3D rigid transformations as well as deformations to efficiently model tip-like structures of ellipsoidal shape. The approach has been successfully applied to accurately localize anatomical landmarks in 3D MR and 3D CT image data. We have also compared the experimental results with the results of a previously proposed 3D differential operator. It turns out that the new approach significantly improves the localization accuracy.

1 Introduction

The localization of 3D anatomical point landmarks is an important task in medical image analysis. Landmarks are useful image features in a variety of applications, for example, for the registration of 3D brain images of different modalities or the registration of images with digital atlases. The current standard procedure, however, is to localize 3D anatomical point landmarks manually which is difficult, time consuming, and error-prone. To improve the current situation it is therefore important to develop automated methods.

In previous work on the localization of 3D anatomical point landmarks, 3D differential operators have been proposed (e.g., Thirion [14], Rohr [12]). Recently, an evaluation study of nine different 3D differential operators has been performed by Hartkens *et al.* [8]. 2D differential approaches for extracting point landmarks in 2D medical images have been described in Briquer *et al.* [3] and Hartkens *et al.* [7]. For other approaches for extracting point landmarks in 2D images, see Walker *et al.* [15] and Likar *et al.* [9]. While being computationally efficient, differential operators incorporate only small local neighbourhoods of an image and are therefore relatively sensitive to noise, which leads to false detections and also affects the localization accuracy. Recently, an approach based on deformable models was introduced (Frantz *et al.* [5], Alker *et al.* [1]). With this approach tip-like anatomical structures are modeled by *surface* models, which are fit to the image data using an edge-based fitting measure. However, the approach

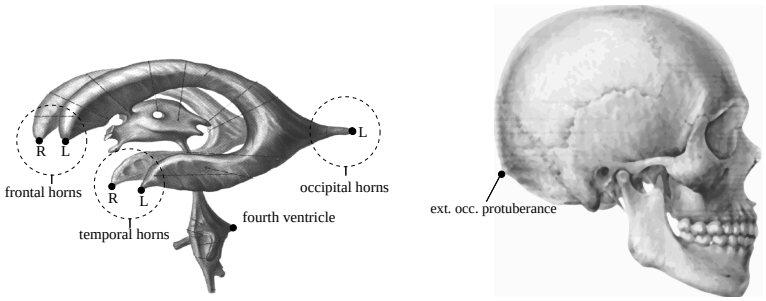

Fig. 1. Ventricular horns of the human brain (from [13]) and the human skull (from [2]). Examples of 3D point landmarks are indicated by black dots.

requires the detection of 3D image edges as well as the formulation of a relatively complicated fitting measure, which involves the image gradient as well as 1st order derivatives of the surface model.

We have developed a new approach for the localization of 3D anatomical point landmarks. In contrast to previous approaches the central idea is to use 3D parametric *intensity* models of anatomical structures. In comparison to differential approaches, larger image regions and thus semi-global image information is taken into account. In comparison to approaches based on surface models, we directly exploit the intensity information of anatomical structures. Therefore, more a priori knowledge and much more image information is taken into account in our approach to improve the robustness against noise and to increase the localization accuracy. In addition, a much simpler fitting measure can be used which does not include the image gradient or derivatives of the model.

This paper is organized as follows: First, we introduce our 3D parametric intensity model (Section 2). Then, we describe the model fitting process (Section 3). Experimental results of applying our new approach to 3D synthetic data and 3D tomographic images of the human head are presented in Section 4.

2 Parametric Intensity Model for Tip-Like Structures

Our approach uses 3D parametric intensity models which are fit directly to the intensities of the image data. These models describe the image intensities of anatomical structures in a semi-global region as a function of a certain number of parameters. The main characteristic, e.g., in comparison to general deformable models, is that they exhibit a prominent point which defines the position of the landmark. By fitting the parametric intensity model to the image intensities we obtain a *subvoxel* estimate of the position as well as estimates of the other parameters, e.g., the image contrast. In [11] such type of approach has been used for localizing 2D corner and edge features.

As an important class of 3D anatomical point landmarks we here consider tip-like structures. Such structures can be found, for example, within the human head at the ventricular system (e.g., the tips of the frontal, occipital, or temporal

horns, see Fig. 1) and at the skull (e.g., the tip of the external occipital protuberance). The shape of these anatomical structures is ellipsoidal. Therefore, to model them we use a (half-)ellipsoid defined by three semi-axes (r_x, r_y, r_z) and the intensity levels a_0 (outside) and a_1 (inside). We also introduce Gaussian smoothing specified by a parameter σ to incorporate image blurring effects. The exact model of a Gaussian smoothed ellipsoid cannot be expressed in analytic form and thus is computationally expensive. To efficiently represent the resulting 3D intensity structure we developed an analytic model as an approximation. This model is based on the Gaussian error function $\Phi(x) = \int_{-\infty}^{x} (2\pi)^{-1/2}\, e^{-\xi^2/2}\, d\xi$ and can be written as

$$g_{Ell.}(\mathbf{x}) = a_0 + (a_1 - a_0)\, \Phi\left(\frac{\sqrt[3]{r_x r_y r_z}}{\sigma} \left(1 - \sqrt{\frac{x^2}{r_x^2} + \frac{y^2}{r_y^2} + \frac{(z + r_z)^2}{r_z^2}} \right) \right) \quad (1)$$

where $\mathbf{x} = (x, y, z)$. We define the tip of the ellipsoid w.r.t. the semi-axis r_z as the position of the landmark, which also is the center of the local coordinate system. In addition, we include a 3D rigid transform $\mathcal{R}$ with rotation parameters (α, β, γ) and translation parameters (x_0, y_0, z_0). The translation parameters define the position of the landmark in the 3D image. Moreover, we extend our model to a more general class of tip-like structures by applying a tapering deformation $\mathcal{T}$ with the parameters ρ_x and ρ_y, and a bending deformation $\mathcal{B}$ with the parameters δ (strength) and ν (direction), which are defined by

$$\mathcal{T}(\mathbf{x}) = \begin{pmatrix} x\ (1 + z\ \rho_x / r_z) \\ y\ (1 + z\ \rho_y / r_z) \\ z \end{pmatrix} \quad \text{and} \quad \mathcal{B}(\mathbf{x}) = \begin{pmatrix} x - z^2 \delta \cos \nu \\ y - z^2 \delta \sin \nu \\ z \end{pmatrix} \quad (2)$$

This results in our parametric intensity model with a total of 16 parameters:

$$g_M(\mathbf{x}, \mathbf{p}) = g_{Ell.}(\mathcal{T}(\mathcal{B}(\mathcal{R}(\boldsymbol{x})))) \quad (3)$$

$$\mathbf{p} = (r_x, r_y, r_z, a_0, a_1, \sigma, \rho_x, \rho_y, \delta, \nu, \alpha, \beta, \gamma, x_0, y_0, z_0) \quad (4)$$

3 Model Fitting Approach

Estimates of the model parameters in (4) are found by a least-squares fit of the model to the image intensities $g(\boldsymbol{x})$ within semi-global regions-of-interest (ROIs), thus minimizing the objective function

$$\sum\nolimits_{\boldsymbol{x} \in \mathrm{ROI}} \left(g_M(\boldsymbol{x}, \boldsymbol{p}) - g(\boldsymbol{x}) \right)^2 \quad (5)$$

Note, the fitting measure does not include any derivatives. This is in contrast to previous fitting measures for surface models which incorporate the image gradient as well as 1st order derivatives of the model (e.g., [5]).

For the minimization we apply the method of Levenberg-Marquardt, incorporating 1st order partial derivatives of the intensity model w.r.t. the model

parameters. The partial derivatives can be derived analytically using the generalized chain rule (e.g., [4]). Note, we do not need to compute the image gradient as is the case with surface models. We need 1st order derivatives of the intensity model only for the minimization process, whereas the surface model approach requires 2nd order derivatives for the minimization.

3.1 Means to improve stability

To improve the robustness as well as the accuracy of model fitting, we separated the model fitting process into three different phases. In the first phase, only a subset of the model parameters are allowed to vary in the minimization process (parameters for semi-axes, rotation, and smoothing). In the second phase, the parameters for the intensity levels and the translation are allowed to vary additionally. Finally, the bending and tapering parameters are included in the third phase.

During model fitting, which is an iterative process, it may happen that the minimizer yields an invalid value for a certain parameter, e.g., a negative value for the smoothing parameter σ or a semi-axis. We developed two strategies to cope with this problem. The first strategy continues the minimization with the last valid parameter vector where the problematic parameter is not allowed to vary for a few iterations. Normally, after a few iterations it is safe to activate this parameter again as the overall parameter vector has changed. Rarely, mainly when using synthetic data, the first strategy does not solve the problem. In this case, the second strategy is applied. With this strategy the last valid parameter vector is modified by slightly changing the value of the problematic parameter towards the invalid value. In our implementation, we use the two strategies alternatingly, always starting with the preferable first strategy (which does not change the parameter values).

3.2 Calibration of the intensity model

Our 3D intensity model in (1) represents an approximation to a Gaussian smoothed ellipsoid. In order to validate our model, we applied the fitting scheme to synthetic 3D images, which have been obtained by discrete Gaussian smoothing of an ideal (unsmoothed) ellipsoid. In these experiments it turned out that we obtain a systematic error in estimating the landmark position. To cope with these errors we developed a nonlinear correction function which "calibrates" the model. The correction function depends on the estimated parameters $\widehat{r}_x$, $\widehat{r}_y$, $\widehat{r}_z$ as well as $\widehat{\sigma}$ and is given by

$$\triangle z_0 = c_1 + c_2\widehat{\sigma} + c_3\widehat{\sigma}^2 + \left(c_4 + c_5\widehat{\sigma} + c_6\widehat{\sigma}^2\right) 2\,\widehat{r}_z\,(\widehat{r}_x + \widehat{r}_y)^{-1} \tag{6}$$

To determine the coefficients $c_1, \ldots, c_6$ we devised a large number of experiments and systematically varied the respective parameters. In total, we used more than 2000 synthetic 3D images (not considering tapering and bending). Incorporating the correction function, we achieved an average localization error of less than 0.2 voxels.

3.3 ROI size selection

From initial experiments it turned out that the used size of the ROI for model fitting has a major influence on the success and the accuracy. If the ROI is too small then we do not incorporate enough image information into the model fitting process to guarantee a successful fitting. On the other hand, if the ROI is too large we might include neighboring structures which negatively influences the estimated parameters. In addition, with an increasing ROI it becomes more likely that our intensity model does not well describe the anatomical structure at hand since a larger part of the structure has to be modelled. As a consequence, the size of the ROI should be well chosen for each landmark in order to improve the results. Also, though the tapering and bending deformations greatly extend the spectrum of shapes that can be modelled, in some cases these deformations tend to decrease the robustness of model fitting. Thus, for each landmark it should be well decided whether the deformations are included or not.

In order to choose an appropriate size for the ROI and decide which types of deformations should be included in the model, we propose the following scheme, which was successfully applied in our experiments. For each landmark, we varied the diameter of the spherical ROI from 11 voxels to 41 voxels in steps of two voxels. For each value of the diameter, we apply our intensity model in four variants: without deformations, with bending deformation only, with tapering deformation only, and with both types of deformations. To gain information about the robustness of model fitting we apply the model fitting for each variant 20 times with different sets of initial parameters. The different parameter sets are obtained by randomly varying the initial values in a range of ± 2 voxels for the semi-axes and translations, ± 8 grey levels for the intensities, ± 0.25 voxels for σ, and ± 0.15 radians for the angles. From these 20 fits we automatically exclude all results which obviously are outliers. These are results with a distance of more than 5 voxels to the initial position, results with an estimated parameter r_z smaller than one or both of the other semi-axes (thus the result is not a tip defined as the location of maximal curvature of the ellipsoid), and results which are drastic outliers, e.g., a semi-axis larger than 1000 voxels or a smoothing value σ of more than 10. Using the remaining fits, we calculated the product of the variances of the three translation parameters as a measure for the robustness of the model fitting w.r.t. different initial parameters.

Finally, we chose the combination of ROI size and deformation variant where the robustness measure was minimal and more than half of the fits were included. Only in one case, namely, the right temporal horn in one image, we accepted the minimum even with less than half of the fits included, because the initialization with the differential operator was very poor. For most landmarks, this simple heuristic leads to a good choice of the ROI size and deformation variant. However, for some landmarks the estimated position was far away from the ground truth position. In these few case, we manually selected the ROI size and the deformation variant, which resulted in an estimated position closest to the initial position and still being sufficiently robust.

Table 1. Size and resolution of the medical 3D images used in the experiments.

Image	Slices	Size in Voxels	Resolution in mm^3
Woho (MR)	sagittal	$256 \times 256 \times 256$	$1.0 \times 1.0 \times 1.0$
C06 (MR)	axial	$256 \times 256 \times 120$	$0.859 \times 0.859 \times 1.2$
C06 (CT)	axial	$320 \times 320 \times 87$	$0.625 \times 0.625 \times 1.0$

4 Experimental Results

Our approach has been applied to 3D synthetic data as well as to two 3D MR images and one 3D CT image of the human head.

4.1 3D Synthetic Data

In the first part of the synthetic experiments we applied our approach to 3D image data generated by the intensity model itself with added Gaussian noise. In total we carried out about 2400 experiments with different parameter settings and achieved a very high localization accuracy with an error in the estimated position of less than 0.12 voxels. We also found that the approach is robust w.r.t. the choice of initial parameters. Additionally, for about 1600 experiments with similar settings but very intense Gaussian noise down to a signal-to-noise ratio of ca. 1, the localization error turned out to be less than 0.52 voxels.

In the second part of the experiments, we used 3D image data generated by discrete Gaussian smoothing of an ideal (unsmoothed) ellipsoid with added Gaussian noise. After applying the correction function (6) we found that the average error in the estimated position was 0.25 voxels. In contrast, the uncorrected position had an average error of 1.25 voxels.

4.2 3D Medical Images

We also applied the new approach to three real 3D tomographic images of the human head (datasets Woho and C06). The sizes and resolutions of the images are listed in Table 1. To achieve isotropic image data in case of the C06 image pair, we applied an interpolation based on 3rd-order polynomials (Meijering [10]) prior to model fitting.

We considered seven tip-like landmarks, i.e. the frontal, occipital, and temporal horns (left and right) as well as the external occipital protuberance. For these landmarks in all three images we used as ground truth, positions that were manually determined in agreement with up to four persons. For the CT image, we did not consider the temporal horns since either the ground truth position was missing due to low signal-to-noise ratio (left horn) or it was not possible to successfully fit the intensity model (right horn). Figure 2 shows the image data in a ROI of the right horn. Particularly with this landmark the image quality was relatively bad. In general, the quality of the CT image at the ventricular system was worse in comparison to the MR images.

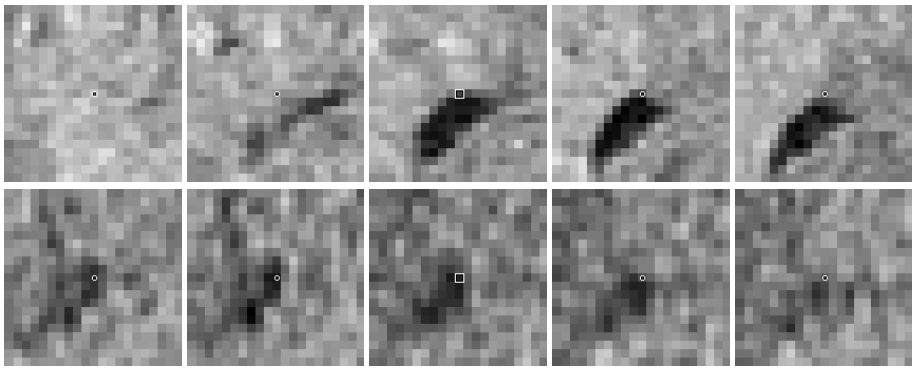

Fig. 2. Five axial 2D slices showing a ROI of $21 \times 21 \times 5$ voxels of the right temporal horn in the C06 image pair (top MR, bottom CT). The ground truth position of the landmark is marked by the square in the center image. The slices on the left are directly below and the slices on the right are directly above the center slice in the 3D image.

Parameter Settings The fitting procedure described above requires the determination of suitable initial parameter values. The specification of these values is an important and not trivial task. Often all parameter values are initialized manually, which is time-consuming. Here, we automatically initialize half of the model parameters. Values for the most important parameters, namely, the translation parameters (x_0, y_0, z_0) defining the position of the landmark were obtained by a 3D differential operator. Here we used the operator $Op3 = det\boldsymbol{C}_g / trace\boldsymbol{C}_g$, where $\boldsymbol{C}_g$ is the averaged dyadic product of the image gradient ([12]). The smoothing parameter σ was always initialized with 1.0 and the deformation parameters ρ_x, ρ_y, δ, and ν were all initialized with 0.0; thus, the intensity model was always initialized as an ellipsoid without deformation. The remaining parameters for the semi-axes (r_x, r_y, r_z), the intensity levels a_0 and a_1, and the rotation angles (α, β, γ) were initialized manually. For the left and right occipital horns in the Woho image, the resulting positions of the 3D differential operator Op3 are relatively far away from the ground truth positions (see Table 4). In addition, the anatomical structure of the occipital horns in this image is rather untypical, thus requiring good initial parameters for successful model fitting. Therefore, we initialized the translation parameters in these two cases manually.

Results Tables 2, 3, and 4 show the fitting results for the considered landmarks. Having chosen the ROI size and the deformation variant we applied the model fitting 100 times with different sets of randomly chosen initial parameters to obtain accurate means and standard deviations of the estimated parameter values. On average, model fitting succeeded for each landmark in 59 out of 100 cases with an average of 75 iterations and a mean fitting error (positive root of the mean squared error) of $\bar{e}_{MFE} = 20.48$ grey levels. For the external occipital protuberance we obtained a relatively large fitting error. Excluding the result for this landmark the mean fitting error improves to $\bar{e}_{MFE} = 10.60$ grey levels. There are two reasons for the larger mean fitting error of the external occipital

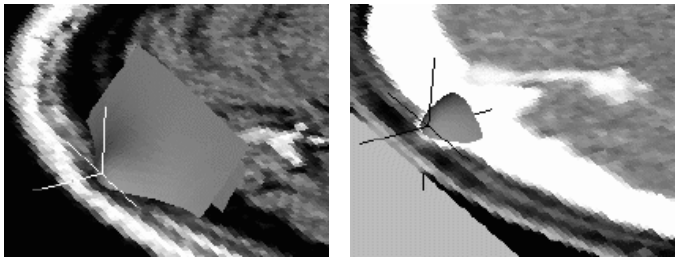

Fig. 3. 3D contour plots of the fitted intensity model for the external occipital protuberance within the original image pair C06 (left MR and right CT). The marked axes indicate the estimated landmark positions. Note, the size of the ROI and the used deformations are different.

protuberance. In case of the CT image, the difference in the intensity levels a_0 and a_1 is more than a magnitude larger than in all other landmarks. Thus, a larger mean fitting error is a consequence. In case of the two MR images, it turns out that our intensity model is not as well suited for this landmark as for the other landmarks. The reason is that the model assumes homogeneous intensities outside of the ellipsoid. In case of the external occipital protuberance which is located directly at the skull, we always find within the ROI three different intensity levels for the intensity a_0, i.e. skin (white and grey) and air (black). Thus, the model has to average these intensities, which explains the relatively large mean fitting error and also causes the larger standard deviations in the position estimates. However, as the estimated landmark position always turns out to be very good, our model is nevertheless applicable and we included the results. We have visualized the results for this landmark for the C06 image pair in Figure 3 using 3D Slicer ([6]). The fitted intensity model is visualized as a contour plot, using the model's intensity at the estimated landmark position as contour value.

The average distance between the estimated landmark positions and ground truth positions for all 19 landmarks computes to $\bar{e} = 1.14mm$. In comparison, using the 3D differential operator Op3, we obtain an average distance of $\bar{e}_{Op3} = 2.18mm$. Thus, the localization accuracy with our new approach turns out to be much better. For the surface model approach ([5]), only comparable data for four landmarks is available, namely, the left and right frontal and occipital horns of the C06 MR image. The average distance of the surface model approach for these four landmarks is $\bar{e}_{Surf} = 1.26mm$, whereas our approach yields $\bar{e} = 0.68mm$ and the differential operator $\bar{e}_{Op3} = 2.17mm$. Bearing in mind the small number of landmarks, we can conclude that the localization accuracy with our new approach is better than the surface model approach, while the differential operator Op3 yields the worst result. Note, the listed distances $\bar{e}$ are not calibrated since for nearly all landmarks deformations were included in the model.

In Figure 4 we visualized the fitting result for the left occipital horn in the C06 (MR) image. Besides the 3D contour plot of the fitted intensity model within three adjacent slices of the original data we also marked the estimated

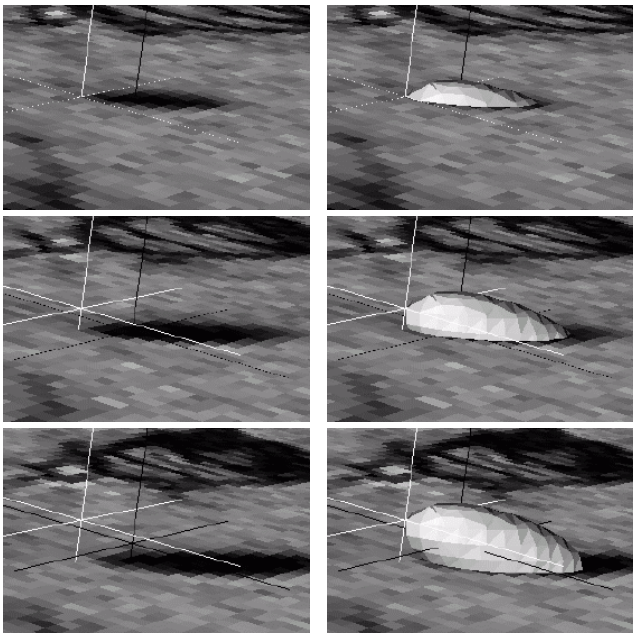

Fig. 4. 3D contour plots of the fitted intensity model for the left occipital horn within the C06 (MR) image. The result is shown with and without the model for three adjacent slices of the original data. The marked axes indicate the estimated landmark positions for the new approach (white) and the differential operator Op3 (black).

landmark positions for the new approach (white) and the differential operator Op3 (black). It can be seen that the model describes the depicted anatomical structures fairly well. Here, the distance between the estimated position of our approach to the ground truth position (not shown) is $0.15mm$ whereas the distance of the differential operator Op3 is $3.32mm$. The estimated position of the differential operator is clearly inside the structure and relatively far away from the tip of the horn. This is a typical result for the long and thin ventricular horns in our experiments. The reason for this systematic localization error results from smoothing the image data when computing the image gradient, which is necessary in order to calculate the response of the differential operator. In contrast, our approach directly exploits the image intensities (without smoothing) and is therefore not vulnerable to this effect.

Also, the figures demonstrate that the spectrum of possible shapes of our intensity model is relatively large. For example, Figure 3 shows a strongly deformed ellipsoid (left) as well as a normal ellipsoid (right) whereas Figure 4 shows a long and thin tapered ellipsoid and Figure 5 shows wider tapered ellipsoids.

The execution time of our algorithm is mainly dependent on the size of the ROI, the chosen variant of the deformation, and the quality of the initial parameters. As a typical example, the fitting time for the right temporal horn in the Woho image including tapering and bending deformations and a diameter of the ROI of 19 voxels is ca. 1s (on a AMD Athlon, 1.7GHz, running Linux).

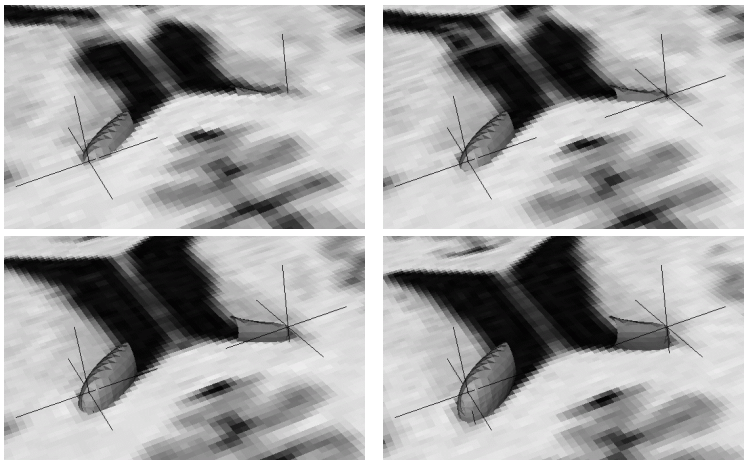

Fig. 5. 3D contour plots of the fitted intensity models for the left and right frontal horn within an MR image (Woho). The result is shown for four different slices of the original data.

5 Discussion

The experiments verify the applicability of our new approach, which yields subvoxel positions of 3D anatomical landmarks. The intensity model describes the anatomical structures fairly well as can be seen from the 3D contour plots. Also, the figures demonstrate that the spectrum of possible shapes of our intensity model is relatively large. Issues for further work are the automatic initialization of all parameters of the model based on differential properties of the image as well as to improve the computational efficiency for selecting the ROI size.

6 Acknowledgement

The original MR and CT images have kindly been provided by Philips Research Hamburg and W.P.Th.M. Mali, L. Ramos, and C.W.M. van Veelen (Utrecht University Hospital) via ICS-AD of Philips Medical Systems Best.

References

1. M. Alker, S. Frantz, K. Rohr, and H.S. Stiehl, "Improving the Robustness in Extracting 3D Point Landmarks from 3D Medical Images Using Parametric Deformable Models", *Proc. MICCAI'2001*, Utrecht, The Netherlands, Oct. 14-17, 2001, *Lecture Notes in Computer Science* 2208, W.J. Niessen and M.A. Viergever (Eds.), Springer-Verlag Berlin Heidelberg 2001, 582-590
2. R. Bertolini and G. Leutert, *Atlas der Anatomie des Menschen. Band 3:Kopf, Hals, Gehirn, Rückenmark und Sinnesorgane*, Springer-Verlag, Berlin, 1982
3. L. Le Briquer, F. Lachmann, and C. Barillot, "Using Local Extremum Curvatures to Extract Anatomical Landmarks from Medical Images", *Medical Imaging 1993:*

Table 2. Fitting results for the ventricular horns and the external occipital protuberance for the C06 image (MR) for ca. 60 experiments. The chosen diameter d of the spherical ROI and the type of deformation are listed. An asterisk marks the landmarks where the robustness criterion was not sufficient to automatically choose d and the deformation type. The estimated landmark position and intensity levels are given together with their standard deviations. Also, the mean fitting error $\bar{e}_{MFE}$ in grey levels and the distance $\bar{e}$ to the ground truth position are listed. For comparison, the distance $\bar{e}_{Op3}$ of the differential operator $Op3$ to the ground truth position is given.

C06 (MR)	d	$\hat{x}_0$	$\hat{y}_0$	$\hat{z}_0$	$\hat{a}_0$	$\hat{a}_1$	$\bar{e}_{MFE}$	$\bar{e}$	e_{Op3}
Left frontal horn	29	150.65	79.58	68.14	91.6	22.3	9.37	1.27mm	1.92mm
(No deformation)*		0.011	0.007	0.004	0.0	0.1			
Right frontal horn	11	112.34	76.85	69.02	93.9	18.8	8.57	0.58mm	1.72mm
(Bending only)*		0.000	0.000	0.000	0.0	0.0			
Left occipital horn	15	143.91	200.85	53.01	84.9	15.2	6.37	0.15mm	3.32mm
(Tapering only)		0.000	0.000	0.000	0.0	0.0			
Right occipital horn	17	107.82	195.98	56.04	86.6	20.0	6.73	0.70mm	1.72mm
(Tapering only)		0.000	0.000	0.001	0.0	0.0			
Left temporal horn	19	164.01	117.26	45.38	82.4	12.8	10.81	1.20mm	1.71mm
(Bending only)		0.482	0.356	0.282	0.2	2.2			
Right temporal horn	13	98.98	112.23	40.63	80.0	18.8	12.43	0.97mm	2.10mm
(Tapering and bend.)*		0.001	0.001	0.000	0.0	0.0			
Ext. occ. protub.	35	130.05	230.94	32.97	61.6	8.7	48.01	0.06mm	1.21mm
(Tapering and bend.)		0.147	0.413	0.562	0.0	5.0			
							Mean	0.70mm	1.96mm

Table 3. Same as Table 2 but for the C06 image (CT). For this image, we restricted the maximal ROI size to 21 voxels as the image only captures a part of the head and therefore three landmarks are close to the image borders.

C06 (CT)	d	$\hat{x}_0$	$\hat{y}_0$	$\hat{z}_0$	$\hat{a}_0$	$\hat{a}_1$	$\bar{e}_{MFE}$	$\bar{e}$	e_{Op3}
Left frontal horn	11	192.80	93.94	77.04	1043.5	996.8	12.92	1.33mm	0.63mm
(No deformation)		0.136	0.086	0.142	0.2	1.5			
Right frontal horn	15	135.31	90.46	78.14	1036.7	1001.8	11.71	1.26mm	2.10mm
(Tapering and bend.)*		0.013	0.005	0.011	0.0	0.0			
Left occipital horn	13	184.07	260.57	69.21	1038.5	989.7	9.65	0.66mm	0.00mm
(Bending only)		0.584	0.390	0.181	0.2	4.2			
Right occipital h.	15	129.50	255.77	72.88	1045.0	994.0	9.83	0.94mm	1.33mm
(No deformation)		0.019	0.170	0.009	0.9	2.0			
Ext. occ. protub.	17	161.20	309.43	48.01	1007.9	2679.0	116.03	1.10mm	1.72mm
(No deformation)		0.002	0.003	0.001	0.1	0.3			
							Mean	1.06mm	1.16mm

Image Processing, 16-19 Febr. 1993, Newport Beach, California/USA, Proc. SPIE 1898, M.H. Loew (Ed.), 549-558

4. I.N. Bronstein and K.A. Semendjajew, *Taschenbuch der Mathematik*, 19. Auflage, Verlag Harri Deutsch, Thun und Frankfurt/Main, 1981
5. S. Frantz, K. Rohr, and H.S. Stiehl, "Localization Of 3D Anatomical Point Landmarks In 3D Tomographic Images Using Deformable Models", *Proc. MICCAI'2000*, Pittsburgh, Pennsylvania/USA, Oct. 11-14, 2000, *Lecture Notes in*

Table 4. Same as Table 2 but for the Woho image (MR).

Woho	d	$\hat{x}_0$	$\hat{y}_0$	$\hat{z}_0$	$\hat{a}_0$	$\hat{a}_1$	$\bar{e}_{MFE}$	$\bar{e}$	$\bar{e}_{Op3}$
Left frontal horn	15	111.26	78.26	101.84	124.0	23.8	9.58	2.22mm	3.16mm
(Tapering only)		0.000	0.000	0.000	0.0	0.0			
Right frontal horn	11	111.49	77.54	132.27	117.3	20.1	8.93	1.44mm	2.24mm
(Tapering only)		0.000	0.000	0.000	0.0	0.0			
Left occipital horn	11	189.38	101.53	91.62	107.3	23.3	10.15	2.31mm	4.12mm
(Tapering and bend.)		0.002	0.001	0.002	0.0	0.0			
Right occipital horn	11	182.63	97.42	150.02	112.7	15.9	7.92	0.68mm	3.61mm
(Tapering only)		0.002	0.003	0.002	0.0	0.1			
Left temporal horn	37	134.90	111.86	88.81	95.1	44.3	21.11	1.80mm	2.83mm
(Tapering only)*		0.301	0.426	0.155	0.0	2.1			
Right temporal horn	19	129.24	114.36	150.16	109.6	35.8	13.49	1.46mm	4.58mm
(Tapering only)		0.045	0.042	0.004	0.0	0.3			
Ext. occ. protub.	29	232.14	149.73	120.96	84.2	26.8	55.54	1.48mm	1.41mm
(Tapering only)*		0.242	0.175	0.571	0.1	0.3			
							Mean	1.63mm	3.14mm

Computer Science 1935, S.L. Delp, A.M. DiGioia, and B. Jaramaz (Eds.), Springer-Verlag Berlin Heidelberg, 2000, 492-501

6. D.T. Gering, A. Nabavi, R. Kikinis, W.E.L. Grimson, N. Hata, P.Everett, F. Jolesz, and W.M. Wells, "An integrated Visualization System for Surgical Planning and Guidance using Image Fusion and Interventional Imaging", *Proc. MICCAI'99*, Cambridge England, Sep. 19-22, 1999, *Lecture Notes in Computer Science* 1679, C. Taylor and A. Colchester (Eds.), Springer-Verlag Berlin Heidelberg, 1999, 808-819
7. T. Hartkens, K.Rohr, and H.S. Stiehl, "Evaluierung von Differentialoperatoren zur Detektion charakteristischer Punkte in tomographischen Bildern", *Proc. 18. DAGM-Symposium Mustererkennung (DAGM'96)*, 11.-13. Sept. 1996, Heidelberg/Germany, *Informatik aktuell*, B. Jähne, P. Geißler, H. Haußecker, and F.Hering (Eds.), Springer-Verlag Berlin Heidelberg, 1996, 637-644
8. T. Hartkens, K.Rohr, and H.S. Stiehl, "Evaluation of 3D Operators for the Detection of Anatomical Point Landmarks in MR and CT Images", *Computer Vision and Image Understanding* 85, 2002, 1-19
9. B. Likar and F. Pernuš, "Automatic Extraction of Corresponding Points for the Registration of Medical Images", *Medical Physics* 26, 1999, 1678-1686
10. E.H.W. Meijering, K.J. Zuiderveld, and M.A. Viergever, "Image Reconstruction by Convolution with Symmetrical Piecewise nth-Order Polynomial Kernels", *IEEE Trans. on Image Processing*, 8(2), 1999, 192-201
11. K. Rohr, "Recognizing Corners by Fitting Parametric Models", *International J. of Computer Vision* 9:3, 1992, 213-230
12. K. Rohr, "On 3D differential operators for detecting point landmarks", *Image and Vision Computing* 15:3, 1997, 219-233
13. J. Sobotta, *Atlas der Anatomie des Menschen. Band 1: Kopf, Hals, obere Extremität, Haut*, Urban & Schwarzenberg, München, 19th edition, 1988
14. J.-P. Thirion, "New Feature Points based on Geometric Invariants for 3D Image Registration", *Int. J. of Computer Vision* 18:2, 1996, 121-137
15. K.N. Walker, T.F. Cootes, and C.J. Taylor, "Locating salient object features", *Proc.* 9^{th} *British Machine Vision Conference (BMVA'98)*, Southampton, UK, Sep., 1998, J.N. Carter and M.S. Nixon (Eds.), volume 2, BMVA Press, 1998, 557-566